We are IntechOpen,
the world's leading publisher of
Open Access books
Built by scientists, for scientists

4,800
Open access books available

122,000
International authors and editors

135M
Downloads

Our authors are among the

154
Countries delivered to

TOP 1%
most cited scientists

12.2%
Contributors from top 500 universities

BOOK CITATION INDEX
CLARIVATE ANALYTICS
INDEXED

WEB OF SCIENCE™

Selection of our books indexed in the Book Citation Index
in Web of Science™ Core Collection (BKCI)

Interested in publishing with us?
Contact book.department@intechopen.com

Numbers displayed above are based on latest data collected.
For more information visit www.intechopen.com

Terahertz Time-Domain Spectroscopy of Metallic Particle Ensembles

Kenneth J. Chau
University of British Columbia
Canada

1. Introduction

The terahertz (THz) frequency range is the region of the electromagnetic spectrum between the microwave and optical bands spanning from 0.1 THz to 10 THz. Historically, electromagnetic radiation in this frequency range has been inaccessible due to the lack of widespread electronic or laser-based radiation sources. Electronic radiation sources such as crystal oscillators are generally confined to operate at frequencies below ~ 100 GHz, while laser radiation sources are generally confined to operate at frequencies above ~ 30 THz. In recent years, the development of femtosecond lasers and quantum electronics have enabled a wide range of implementations to both generate and detect THz radiation [14]. One of the earliest and most widespread techniques is THz time-domain spectroscopy. THz time-domain spectroscopy is based upon the generation of a broad-band, free-space THz transient, which is detected using a femtosecond pulse to sample the THz electric field in the time-domain. THz spectroscopic measurements are performed by illuminating materials with a THz pulse and measuring the pulse after reflection from or transmission through the material. The electromagnetic properties of the material are inferred from changes in the amplitude and phase of the measured electric field pulse relative that of the incident electric field pulse. THz time-domain spectroscopy has been applied in transmission mode to characterize the THz-frequency optical constants of dielectrics and superconductors [5, 8, 15, 16] and in reflection mode to characterize the reflection amplitude and associated phase change due to semiconductors such as InSb [6] and highly doped silicon [17, 18].

The implementation of THz time-domain spectroscopy requires that the reflected/ transmitted THz pulse undergo measurable transformation upon interacting with the material; spectroscopic measurements made in transmission mode require that the investigated material exhibit partial transparency to THz radiation (that is, some radiation must pass through the material), while spectroscopic measurements made in reflection mode require that the material exhibit partial reflectance to THz radiation (that is, the reflected radiation must be altered relative to the incident radiation). Highly reflective materials such as bulk metals are not amenable to THz time-domain spectroscopy in either transmission or reflection modes. Due to the large and negative real part of the relative permittivity of most metals at THz frequencies (where typically $\mathrm{R}e[\underline{\varepsilon}(\omega) \sim -10^5]$), incident THz radiation penetrates only a short, subwavelength distance $\delta \sim 100\mathrm{nm}$ into the surface of the metal and nearly all the incident electromagnetic energy is reflected. The high

reflectivity of bulk metals at THz frequencies precludes transmission-based measurements, and the short penetration distance of THz electromagnetic radiation into bulk metal limits the amplitude and phase change observable in a reflection measurement.

While bulk metals (defined as materials composed of a continuous, conducting medium with physical dimensions much greater than the wavelength) are completely opaque to THz radiation, dense collections of subwavelength sized metallic particles have been shown to exhibit partial transparency at THz frequencies [2, 3]. This transparency is unexpected since the particles that constitute the ensemble are composed of a material that is opaque to THz radiation and the particles are densely packed in a manner which precludes direct THz propagation through the ensemble. The objective of this Chapter is twofold: 1) we will explore the physical mechanisms underlying the THz transparency of metallic particle ensembles through experimental evidence supported by simulation and 2) we will demonstrate the application of THz time-domain spectroscopy to study the effective optical constants of a metallic sample. First, the THz electromagnetic response of a single, isolated metallic particle is modeled using finite difference time-domain (FDTD) calculations of the Maxwell Equations. FDTD calculations are then applied to model THz electromagnetic wave interaction with a dense collection of metallic particles, where it is shown that THz electromagnetic propagation through the particle ensemble is mediated by near-field electromagnetic coupling between nearest-neighbor particles across the ensemble. The influences of the extent of the ensemble L and the particle size d on the THz transparency are experimentally tested using THz time-domain spectroscopy in transmission mode and the experimental evidence is compared with numerical simulations based on FDTD calculations. THz time-domain spectroscopy is then applied in transmission mode as a non-invasive, direct probe of the effective dielectric properties of a metallic particle ensemble. The sensitivity of this methodology for probing metallic media is tested by monitoring the properties of the ensemble during the liquid-solid phase transition of the metallic medium.

2. Single subwavelength metallic particle

The electromagnetic response of a single, subwavelength metallic particle excited by a THz electromagnetic wave is governed by two sequence of events: 1) the THz electromagnetic wave incident on the particle surface penetrates $\delta \sim$ 100nm into the metal where it induces charge motion and subsequently, current density, and 2) a dipolar electric field, also known as a particle plasmon, is formed by the accumulation of negative and positive charge at opposite sides of the particle's surface. At the surface of the particle, the dipolar electric field induced by excitation of the particle is oriented normal to the particle surface and has a net orientation along the direction of the incident electric field.

To visualize the electric fields associated with the THz particle plasmon, the electromagnetic response of a single, isolated subwavelength metallic particle to electromagnetic wave excitation is studied using the FDTD method to solve the Maxwell equations in two dimensions. In the FDTD method, the material properties of each spatial grid point in the simulation space are independently specified, and the complete spatial and temporal evolution of the electric and magnetic fields are solved. Shown in Fig. 1 is a series of snapshots of the electric field amplitude distribution obtained from an FDTD calculation describing a THz electromagnetic pulse (with spectral contents centred at 0.6 THz and a 1 THz bandwidth) incident on a single copper particle having a diameter d = 75 μm immersed in free-space. In the calculations, the THz pulse propagates upward from the bottom of the

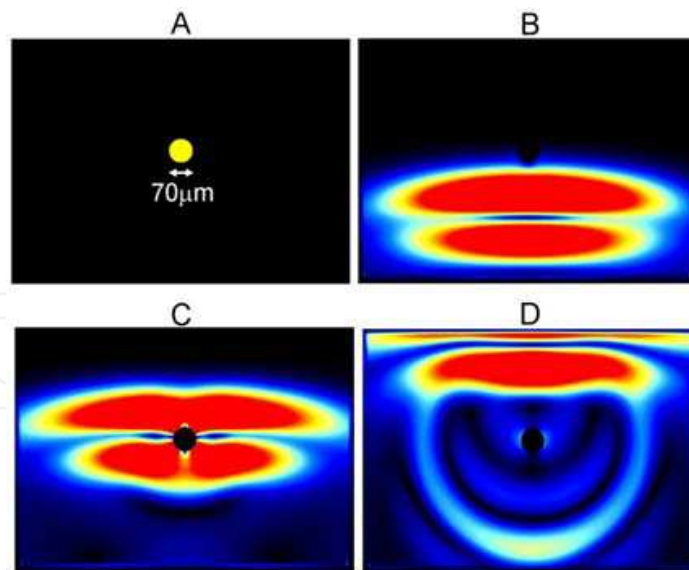Fig. 1. Images of a FDTD calculation modeling single-cycle THz pulse excitation of an isolated 75 μm diameter copper particle (A) prior to excitation, (B) at 0.0 ps, (C) at 3.5 ps, and (D) at 8.5 ps.

images and is polarized in the plane of the images (transverse magnetic or TM). The images in Fig. 1B to 1D correspond to snapshots of the THz electric field magnitude at various times in the progression of the simulation. At $t = 0.0$ ps, the single-cycle polarized THz pulse propagates towards the subwavelength sized metallic particle, and when the THz pulse overtakes the particle at 3.5 ps, negligible THz electric field amplitude is present inside the particle, since the skin depth (penetration distance) of the THz electromagnetic wave is significantly less than the particle diameter. At 3.5 ps, the electric field amplitude can be conceptually divided into contributions from the external THz pulse and the electric field amplitude arising from the induced charges at the particle's surface. In this frame of the simulation, it is not possible to separate the external and induced-charge contributions to the total electric field amplitude. After the passage of the THz electric field pulse at 8.5 ps of the simulation, the electric field amplitude (Fig. 1D) and vector electric field (Fig. 2A) arising from the charges induced on the particle by the external electromagnetic wave can be visualized. At this snapshot after the THz pulse has propagated past the particle, the remnant electric field around the particle is confined to the surface and exhibits dipole-like signatures. Such a surface field is attributed to the excitation of charge oscillations on the particle oriented along the polarization of the external THz electric field. By taking the divergence of the electric field distribution, the charge density distribution associated with the dipolar electric fields can be obtained. As shown in Fig. 2B, the induced charge density illustrates dipolar charge induction by the incident THz pulse, where positive and negative charge density accumulate at opposing sides of the particle along the direction of the incident THz pulse polarization. The induced charge densities are coupled to an electromagnetic field confined to the surface of the particle. The dipolar electric field (highlighted in Fig. 3) associated with the induced charge density is strongest directly above the surface of the particle and decays exponentially within a distance of $\simeq 250$ μm. This distance is less than the central wavelength of the THz pulse, $\lambda = 500$nm, indicating that the surface fields are confined to within a subwavelength region in the vicinity of the particle.
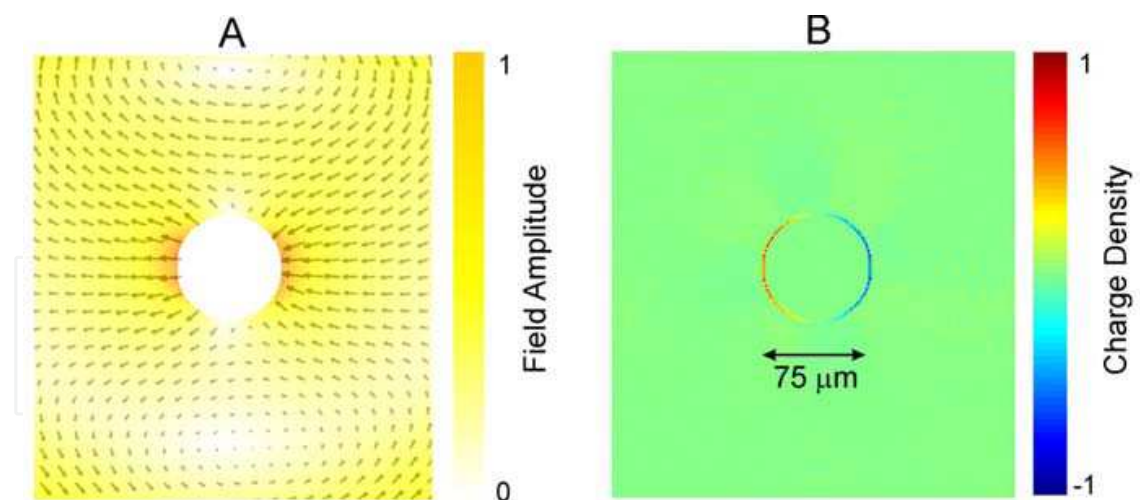
Fig. 2. (A) Vector plot of the electric field in the vicinity of a 75 μm copper particle after excitation by a single-cycle THz pulse at 8.5 ps of the simulation shown in Fig. 1. (B) illustrates the corresponding dipolar charge distribution at the surface of the particle.
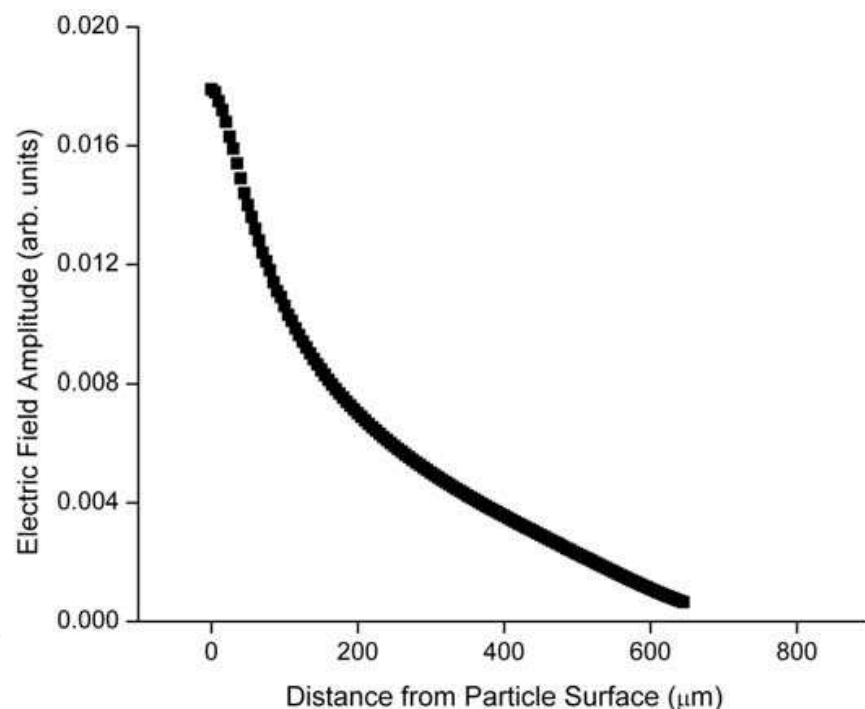

Fig. 3. Calculated amplitude of the electric field outside the surface of a 75- μmdiameter copper particle after excitation by a single-cycle THz pulse (which has propagated past the particle) with respect to the distance from the particle surface.

3. Ensemble of subwavelength metallic particles

In a collection of closely-spaced subwavelength metallic particles, electromagnetic interaction between the particles plays an important role in the overall electromagnetic properties of the ensemble. Since the particles are electromagnetically coupled, each particle is excited by the external electric field in addition to the field scattered from all the other particles. The complex interactions between metallic particles make it difficult to analytically

describe the electromagnetic properties of the ensemble. One common technique to determine the electromagnetic properties of subwavelength metallic particle collections is via effective medium approximations [1, 11]. The effective medium approximation replaces an inhomogeneous medium with a fictitious homogeneous effective medium which expresses the linear response of the whole inhomogeneous sample to an external electric field. Thus, rather than laboriously describing the microscopic interactions between the constituents, the entire heterogeneous medium is described by a single effective parameter. Effective medium approximations have been employed to derive the homogeneous optical parameters of metallic clusters and metamaterials with subwavelength features [19]. The validity of effective medium approximations is governed by the quasi-static approximation, wherein the electric and displacement fields throughout the heterogeneous medium must be approximately uniform. To illustrate, consider a subwavelength metallic sphere having a diameter of d. The sphere is centred at $z = 0$ and illuminated by an electromagnetic plane-wave from free-space. For the field amplitude within the particle to be uniform, there must be minimal absorption over the particle dimension, or

$$x\text{Im}[\sqrt{\underline{\epsilon}(\omega)}] \ll 1 \tag{1}$$

where $\text{Im}[\sqrt{\underline{\epsilon}(\omega)}]$ is the imaginary part of the complex refractive index of the metal and $x = \pi d/\lambda$ is the size parameter. Similarly, there must be minimal spatial variation of the electromagnetic wave in the sphere, which implies that the wavelength inside the sphere is much greater than the particle size, or

$$x\text{Re}[\sqrt{\underline{\epsilon}(\omega)}] \ll 1 \tag{2}$$

where $\text{Re}[\sqrt{\underline{\epsilon}(\omega)}]$ is the real part of the refractive index of the metal. Combining the inequalities Eqs. 1 and 2 gives the condition in which the quasi-static regime is valid

$$x\left|\sqrt{\underline{\epsilon}(\omega)}\right| \ll 1 \tag{3}$$

Eq. 3 can be applied to test the applicability of field-averaging for micron-scale particles excited by electromagnetic waves at THz frequencies. Assuming a spherical copper particle with a diameter of 75 μm and a metal permittivity $\underline{\epsilon}_{Cu}(\omega)$ (1 THz) $\simeq -10^4 + -10^5$ excited by an electromagnetic wave with a wavelength of 300 μm (corresponding to a frequency of 1 THz)

$$x\left|\sqrt{\underline{\epsilon}_{Cu}(\omega)}\right| = 248 > 1. \tag{4}$$

Thus, field averaging techniques to derive effective homogeneous parameters cannot be applied to describe the optical properties of micron-scale metallic particle at THz frequencies. Since field-averaging cannot be used to effectively homogenize the THz electromagnetic response of the dense metallic particle ensembles, electromagnetic interactions within the ensemble are simulated rigorously using FDTD calculations of the Maxwell Equations in two dimensions. The structure used in the simulation is a randomly generated ensemble of copper particles in an air ambient that have a circular cross section with a diameter $d = 75$

μm. The particles are randomly packed to achieve a packing fraction p = 0.56 and the ensemble size is 5mm × 5mm, as depicted in Fig. 4A. In the simulations, a single-cycle THz pulse (with spectral contents centred at 0.6 THz and a 1 THz bandwidth) is normally incident on a flat face of the ensemble and the transmission through the opposing flat face of the ensemble is measured.
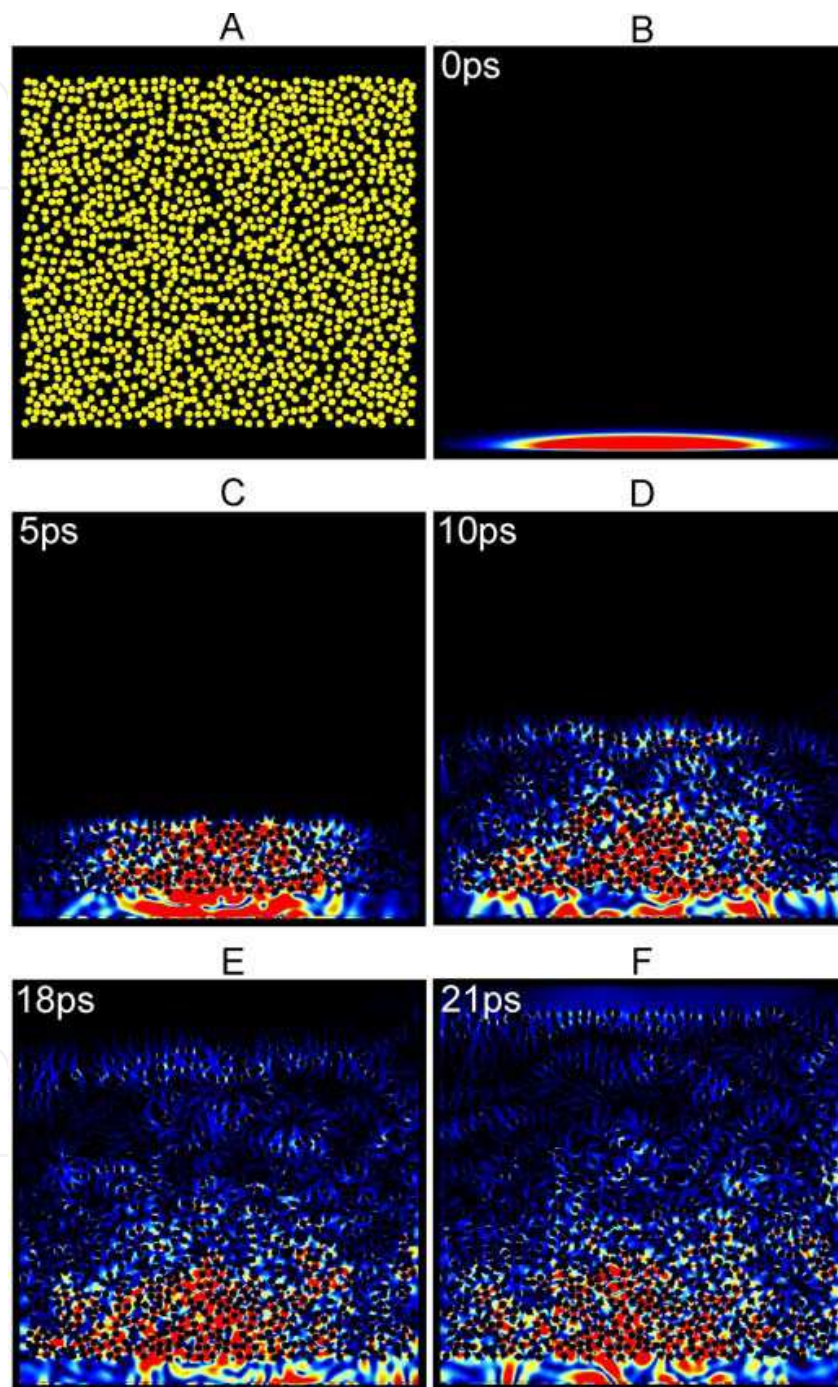

Fig. 4. (A) Simulation geometry in which an ensemble of 75- μm diameter copper particles with a volume fill fraction of 0.56 is excited by a TM-polarized THz electromagnetic pulse. Snapshots of the THz electric field magnitude within a random 5mm × 5mm ensemble of copper particles at times (B) 0 ps, (C) 5 ps, (D) 10 ps, (E) 18 ps, and (F) 21 ps.

Examination of the dynamics of the internal electric field amplitude obtained from the FDTD calculations shed insight into the mechanism underlying the propagation of THz electromagnetic energy through the particle ensembles. Figs. 4B to 4F depict snapshots of the spatio-temporal evolution of the electric field amplitude due to excitation of the L = 5mm ensemble by the THz pulse at representative times, t. At t = 0 ps, the polarized THz pulse is incident on the particle ensemble, and at t = 5 ps, the pulse couples into particle plasmons on the individual particles, evidenced by the high electric fields near the surfaces of the particles. The snapshots at time t = 10 ps and t = 18 ps show that significant electromagnetic energy is squeezed in the free-space gaps between the particles, while there is negligible field penetration into the individual particles. Collectively, the particles carry electromagnetic energy over the extent of the ensemble, evidenced by a wave-front which appears in the simulation as a large-electric-field-amplitude band progressing through the medium. By tracking the wavefront as it advances through the system, an electromagnetic energy velocity of $0.51c$ is measured. At t = 21 ps, this leading wave-front approaches the far boundary of the ensemble and radiates into free-space. The simulations demonstrate that a THz electromagnetic wave in a dense metallic particle ensemble is squeezed into the subwavelength-scale interstitial gaps of the metallic particle ensembles, yet can propagate through large, millimetre-scale distances and at the back face of the ensemble, radiate into free-space.

4. THz time-domain spectroscopy of metallic particles

In this section, the THz electromagnetic properties of an ensemble of subwavelength sized copper particles are studied using THz time-domain spectroscopy in transmission mode. The metallic particle ensemble consists of pure copper particles that are spherical in shape and nearly mono-dispersed in size, with a mean particle diameter d = 75 μm and a volume metal packing fraction (volume ratio of metal to the entire volume of the ensemble) p = 0.51 immersed in air. A scanning electron microscope image of a dispersed collection of the particles is shown in Fig. 5. The THz transmission through the particle ensemble is measured with the experimental configuration depicted in Fig. 6. Single-cycle, linearly polarized THz pulses, with spectral contents centred at 0.6 THz and a 1 THz bandwidth, are generated from a GaAs photoconductive switch excited with focused < 20 fs, 800 nm laser pulses supplied from a Ti:Sapphire laser at a repetition rate of 80MHz. The collimated THz beam is directed towards a sample cell, which is composed of THz-transparent polystyrene windows with variable separation distance L, that houses the metallic particle ensemble. The time-domain electric field transmission in addition to polarization of the transmission is measured to characterize electromagnetic wave transport through the medium. The on-axis THz electric field pulse transmitted through the ensemble is coherently detected via an optically gated 500 μm thick ⟨111⟩ ZnSe electrooptic crystal, and time-resolved information is obtained by varying the delay between the THz pulse and a sampling probe pulse.

Significant THz transmission through the particle ensemble is measured for sample thicknesses, L, up to 7.7 mm, where nearly 20% transmission is observed for the thinnest L = 0.6-mm ensemble. Fig.7 depicts the time-domain THz electric field pulses transmitted through particle ensembles over the range 0.6mm ≤ L ≤ 7.7 mm referenced to the
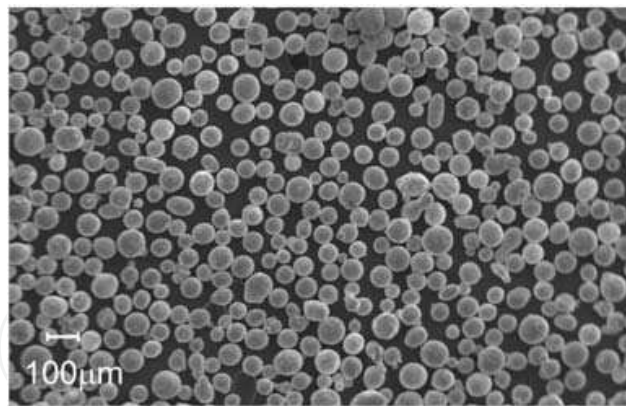
Fig. 5. Scanning electron microscope image of a dispersed collection of copper particles with an average diameter of 75 μm.
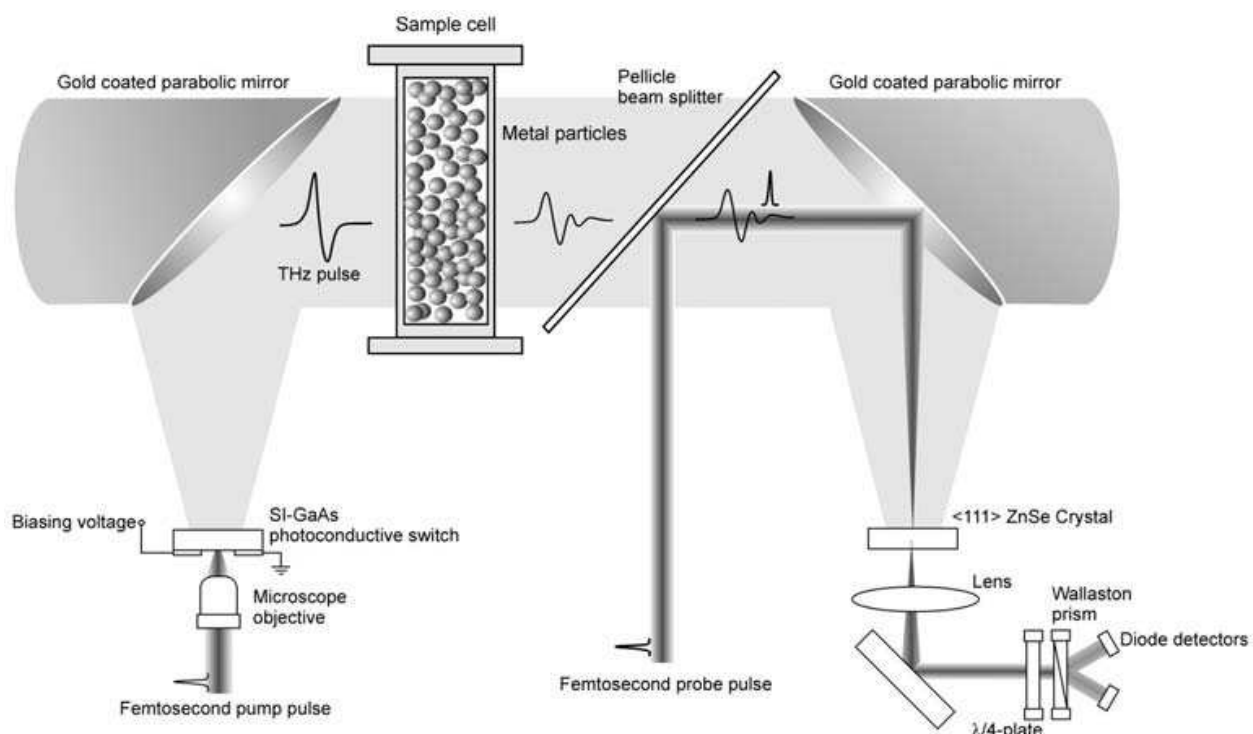

Fig. 6. Schematic of the free-space THz generation and electro-optic detection setup used to characterize the THz electric field transmission through the metallic particle ensembles.

transmission through an empty sample cell. Due to the opacity of the particles, the subwavelength-scale of both the particle size and average inter-particle spacing, and the long extent of the ensemble relative to the wavelength, the measured THz transmission cannot arise from direct, line-of-sight electromagnetic propagation through the particles. In general, the time-resolved signals are characterized by several broad oscillations, which are relatively delayed as L increases. The reference pulse (corresponding to the pulse that is incident on the ensembles) is localized in time (within ~ 1 ps); upon impulsive excitation of the sample, it requires a finite time for energy to propagate through the sample. To estimate the energy propagation velocity from one end to the sample to the other end, the relative delay of the transmitted field is measured. Here, the delay corresponds to the time difference between the centroid of the time-domain intensity distribution of the reference
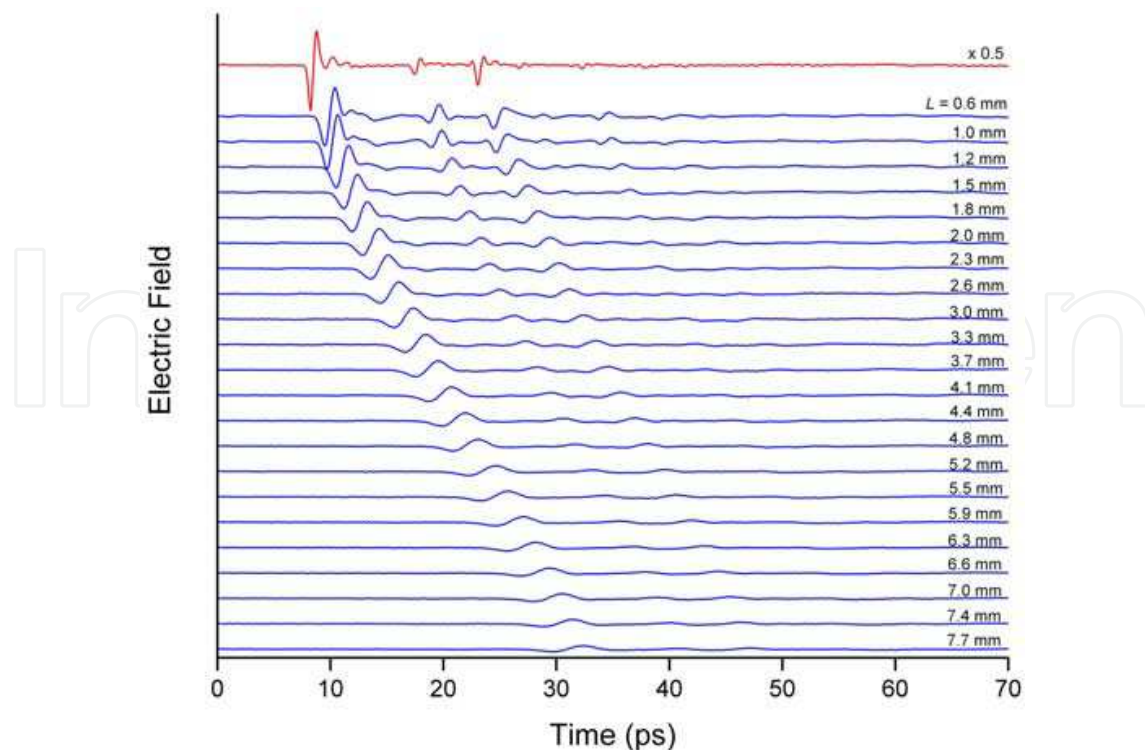
Fig. 7. Time-domain waveforms of the far-field THz transmission through ensembles of copper particles with lengths ranging from L = 0.6 mm to L = 7.7 mm.

pulse and the centroid of the time-domain intensity distribution of the transmitted pulse. Shown in Fig. 8 is the relative pulse delay as a function of sample thickness, referenced to an equivalent air path. The measured delay translates to an electromagnetic energy velocity of 0.51±0.01c or an effective refractive index of 2.0±0.1. It should be noted that the effective macroscopic index reported here describes the overall response of the metallic particle ensemble to THz electromagnetic wave excitation, but is not derived from the effective medium approximation. As L increases from 0.6 to 7.7 mm, the durations of the transmitted electric field pulses are broadened from 2 ps to 6 ps. The pulse broadening, which increases with larger values of L, is indicative of a preferential amplitude reduction in the higher frequency components of the incident pulse. Due to the absence of significant intrinsic material resonances for bulk copper at THz frequencies, the preferential loss of higher frequency components likely originates from the scattering due to the extrinsic structural characteristics of the random metallic medium.

The experimentally measured relative delay of the THz transmission is compared with results obtained from FDTD calculations in Fig. 8. It should be noted that the packing fraction of the sample in the calculations (0.56) is larger than the experimentally measured packing fraction of the sample used in the experiments (0.51). Augmenting the packing fraction in the two-dimensional system in the simulations effectively increases the surface area of the particles, which more accurately accounts for non-radiative losses occurring at the surface of the three-dimensional particles used in the experiments. As shown in Fig. 8, the relative delay of the THz transmission obtained from FDTD calculations demonstrates excellent agreement with experimental observations. The linear increase in the relative delay with respect to the sample thickness indicates that the THz transmission is mediated by a phase accrual across the length of the ensemble. By increasing the length of the sample, the

THz electromagnetic wave interacts with a greater number of particles, which augments the delay in the measured transmission.
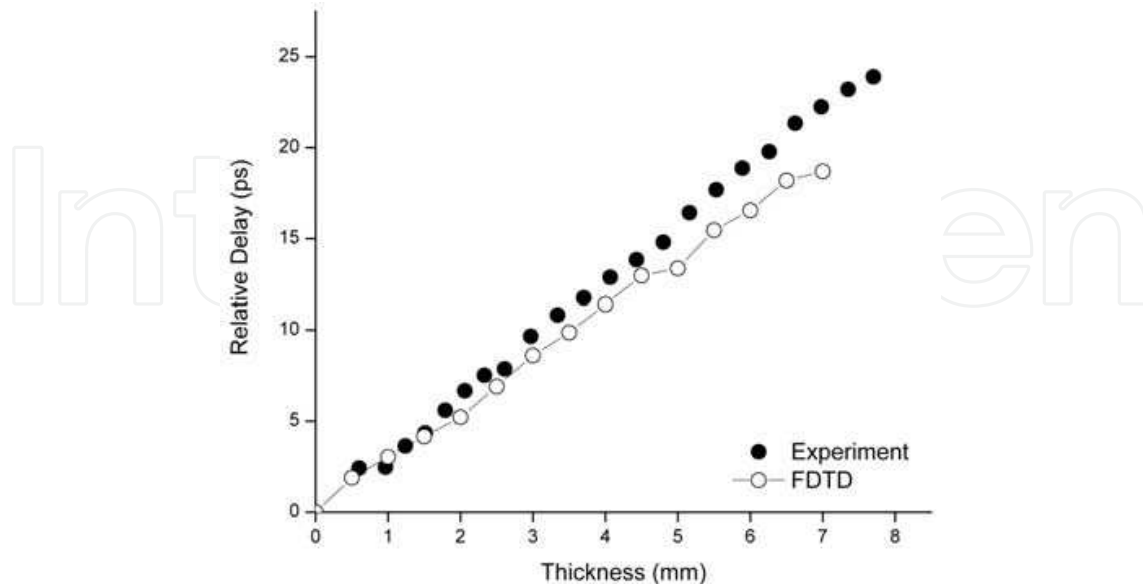

Fig. 8. The relative delay of the transmitted THz pulse through the copper ensembles with respect to the thickness of the ensemble obtained from experiment and simulation.

The polarization of the electric field transmitted through the particle ensemble provides further insights into the origin of the THz transmission. Comparison of the polarization of the transmitted THz pulse with the linear polarization of the incident THz pulse maps the degree of coherence of electromagnetic energy transport across the ensemble by onto a polarization change. A high correlation between the incident and transmitted polarizations would indicate a high degree of electromagnetic coupling between the incident and transmitted electric fields, whereas a low correlation would indicate a low degree of coupling. The transmitted electric field polarization is characterized by varying the angular orientation of the optical axis of the ⟨111⟩ ZnSe crystal electro-optic detector relative to the probe polarization. Fig. 9 illustrates polar plots of the intensity distribution of the free-space THz pulse incident onto the sample, in addition to those of the transmitted THz pulse through 2.2-mm thick and 7.7-mm thick ensembles of copper particles. The ensembles are composed of copper particles that have a mean diameter of 75 ± 5 μm and a packing fraction of 0.51 ± 0.05. As highlighted in Fig. 9B, the THz electric field pulse transmitted through the 2.2-mm thick ensemble shows a high degree of polarization preservation of the incident horizontal, linear polarization of the incident pulse. As the sample thickness increases to 7.7mm (Fig. 9C), the transmission becomes more unpolarized. Polarization preservation of the transmission through the 2.2-mm thick ensemble indicates that at this thickness value, the THz transmission is predominantly mediated by coherent coupling across the ensemble. The diminishing polarization purity of the transmission as the sample thickness increases to 7.7 mm is attributed to augmented scattering of the THz electromagnetic wave, which randomizes the polarization and impairs the correlation between the incident and transmitted electric fields. From the data, it is inferred that the coherence length of electromagnetic transport across the ensemble, delineating a length scale below which the incident and transmitted electric fields are highly correlated, is on the order of several millimetres.
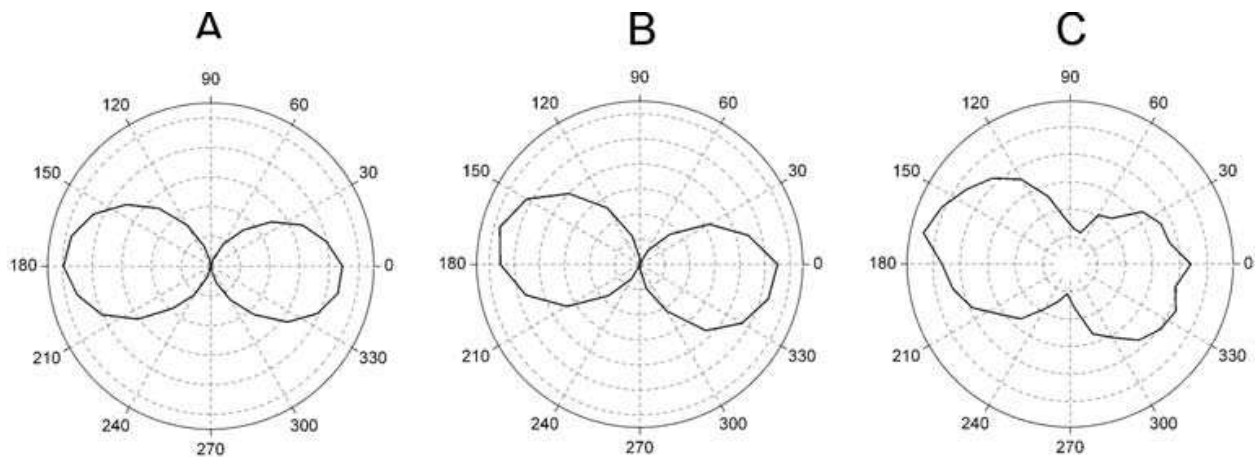
Fig. 9. Polar plot of the intensity distribution of (A) the incident THz pulse and the transmitted THz pulse through (B) a 2.2-mm thick and (C) a 7.7-mm thick ensemble of copper particles.

When a THz electromagnetic wave is incident on a subwavelength sized particle, a portion of the incident energy is coupled into the particle plasmon (as illustrated by simulation in Section 1) and a portion of the incident energy is scattered by the particle. Intuitively, the amount of electromagnetic energy "lost" to scattering from the metallic particle should be proportional to the cross-sectional area of the particle. As the particle cross sectional area increases, a larger portion of the incident electromagnetic energy is reflected and less electromagnetic energy is coupled into the localized particle plasmon at the surface of the particle. In the limit where the cross-sectional area of the particle is infinite, the incident electromagnetic wave encounters a bulk metallic surface and is completely reflected. To further investigate the origin of the THz transparency of metallic particle ensembles, the influence of the particle size on the THz transmission is studied. The relationship between the particle size of the ensemble and the THz transparency of the ensemble is studied using THz time-domain spectroscopy in transmission mode, where the THz electric field transmission is measured through several particle ensembles of fixed length (and fixed packing fraction) composed of copper spheres with average diameters of 85 ± 9 μm, 194 ± 9 μm, 250 ± 10 μm, 283 ± 8 μm, 372 ± 17 μm, 462 ± 17 μm, 560 ± 15 μm, and 670 ± 30 μm. In reporting the particle sizes, the nominal size corresponds to the average particle diameter and the error represents one standard deviation.

Shown in Fig.10 are the time-domain waveforms, the associated Fourier spectra, and the total integrated power of the transmission through copper particle ensembles where the particle sizes range from 85 ± 9 μm to 670 ± 30 μm. The thickness of the ensemble is kept constant at $L = 3.0$ mm throughout the experimentation. As the average particle size increases from 85 μm to 372 μm, the THz electric field transmission amplitude is dramatically reduced and is nearly zero for particles with diameters exceeding 462 μm. Associated with this attenuation is a shift in the central frequency of the transmission from 0.1 THz to 0.08 THz, indicating a preferential attenuation of the higher frequency components of the THz pulse (Fig. 10B). The preferential attenuation associated with the increasing particle size is due to the frequency-selective particle plasmon response of the particles. As the particle size increases, the shorter wavelength (higher frequency) components of the incident THz pulse cannot efficiently polarize the individual particles

and do not excite the particle plasmon mode. As a result, the higher frequency components do not couple across the medium and are not radiated into the far-field.
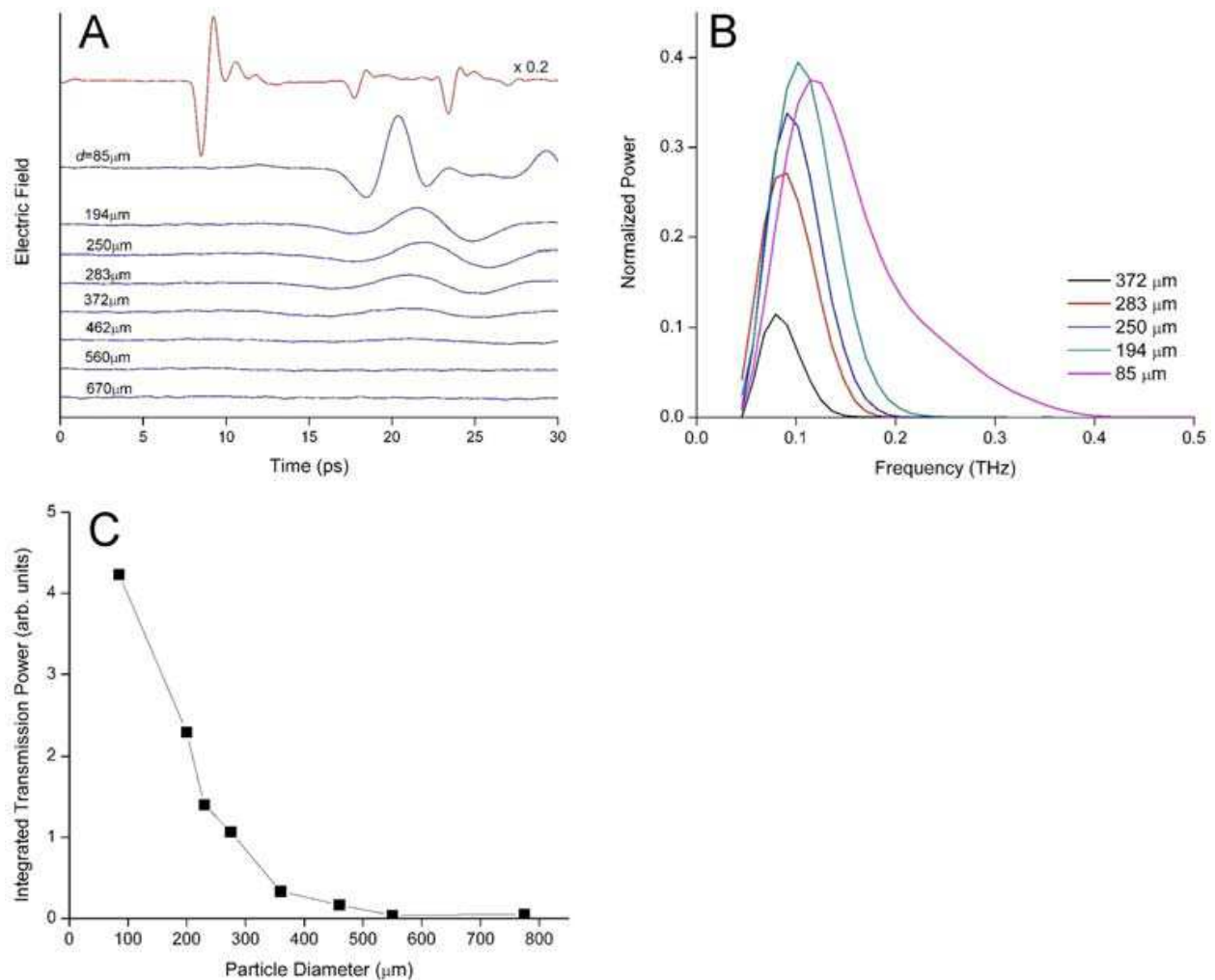

Fig. 10. (A) Time-domain waveforms of the far-field THz transmission through a 3.0-mm thick ensemble of copper particles with average particle diameters ranging from 85 μm to 670 μm. (B) Power spectra of the transmission through the particle ensembles normalized by the power spectrum of the incident THz pulse. (C) Total integrated transmitted power through the particle ensembles with respect to the average diameter of the particles that constitute the ensemble.

Fig.11 illustrates polar plots of the intensity distribution of the transmitted THz radiation through a L = 3 mm thick ensemble of densely-packed copper particles with mean diameters of 85 μm, 283 μm, and 372 μm. For the ensemble of 85- μm diameter particles, the transmission polarization preserves the incident linear polarization, indicating a high degree of electromagnetic coupling across the ensemble. The diminished polarization of the transmission through the ensemble of 283- μm diameter particles indicates reduced electromagnetic coupling. This observation coincides with a four-fold reduction in the transmitted intensity through the ensemble of 283- μm diameter particles relative to that of the 85- μm diameter particles.
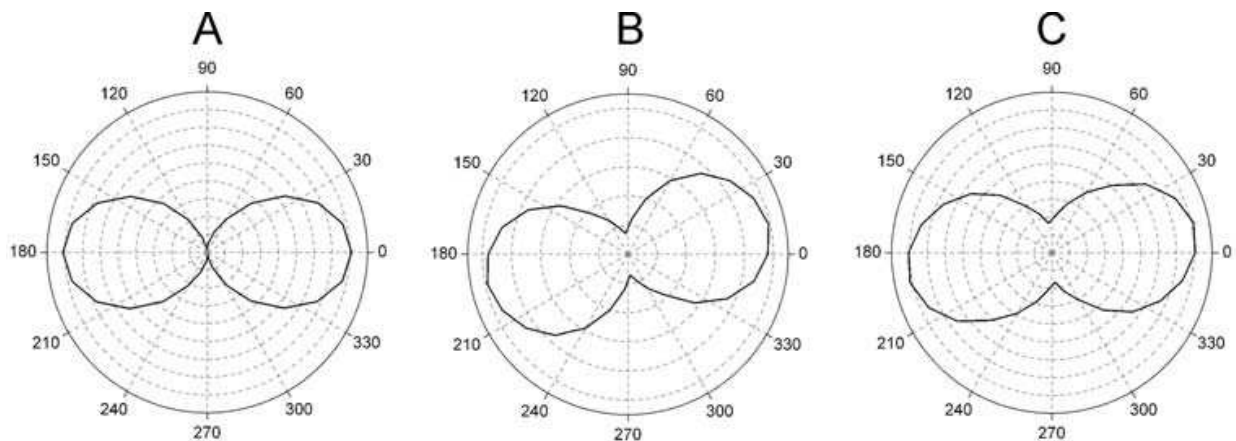
Fig. 11. Polar plot of the intensity distribution of the THz pulse transmitted through a 3.0-mm thick ensemble of copper particles with average diameters of (A)85 μm, (B)283 μm, and (C)372 μm.

The transmission through the ensemble of 372- μm diameter particles is nearly unpolarized, indicating that the transmitted energy is not coherently channeled across the extent of the ensemble. For the ensemble of 372- μm diameter particles, the transmitted intensity is almost fully extinguished.

The effect of the particle diameter on the polarizability of a single, isolated metallic particle (which is indicative of the degree of coupling to the particle plasmon mode of the particle) is illustrated via FDTD calculations of two situations in which a single, isolated metallic particle with a diameter of either 75 μm or 200 μm is excited by a THz electromagnetic pulse from free-space. The excitation pulse is a single-cycle THz transient centred at 0.6 THz with a 1 THz bandwidth, matching the THz pulses employed in previous experiments and simulations. In these simulations, the single-cycle THz pulse propagates upward toward the metallic particle. To map out the charge density induced by the external THz electric field pulse, the induced charge density distribution is calculated by taking the divergence of the vector displacement field distribution. Fig. 12 illustrates the instantaneous induced charge density distribution at the surface of the two particles after THz pulse excitation taken at the same time. For the 75- μm diameter particle, the THz electric field pulse induces a dipolar charge density distribution where conduction electrons at the surface of the two halves of
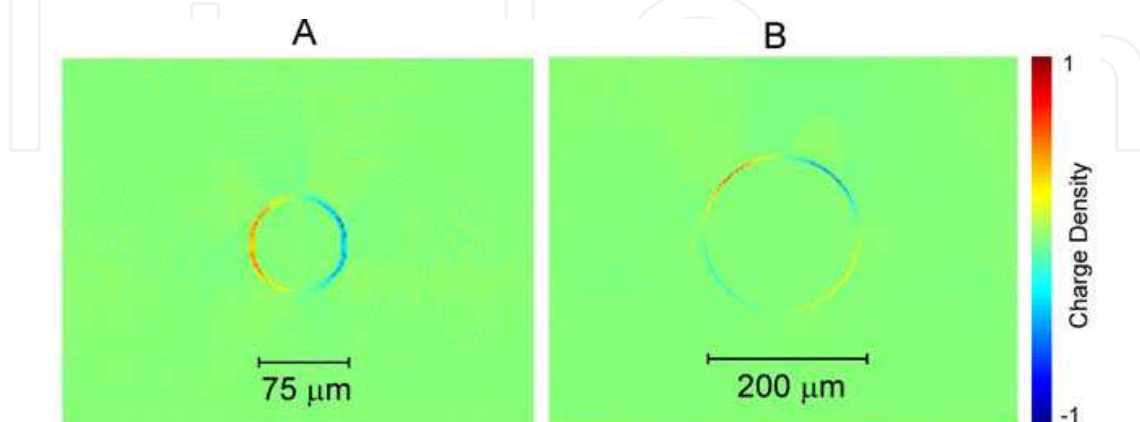

Fig. 12. FDTD calculation of the induced charge density distribution of a (A) 75- μm diameter particle and (B) 200- μm diameter particle after excitation by a single-cycle THz pulse in free-space.

the particle oscillate anti-parallel. As the particle size increases to 200 μm, the predominant polarization mode induced by the THz electric field pulse is quadrupolar. The magnitude of the charge density distribution for the larger particle is significantly weaker than the dipolar charge density distribution of the smaller particle. The peak charge density of the quadrupolar distribution is reduced to $\simeq 0.6$ relative to the peak charge density of the dipolar distribution. The larger metallic particle is not efficiently polarized by the incident THz pulse, since a significant portion of the incident pulse is reflected by the larger particle and only the lower frequency components of the pulse can polarize the particle. In an ensemble of particles, this effect leads to a preferential reduction in the transmission of higher frequency components and an overall reduction in the total transmitted power.

5. Phase-transition THz spectroscopy of metallic particles

Terahertz time-domain spectroscopy is applied to study intrinsic, temperature-dependent phase transitions in a metallic particle ensemble. A phase transitions is defined as a transformation of a thermodynamic system from one phase to another. A distinguishing feature of phase transitions is an abrupt change in one or more physical properties of the material with a small change in a thermodynamic quantity such as temperature. For instance, when the specific energy of a metal is raised to the latent heat of fusion, the metal changes from the solid phase to the liquid phase. The microscopic mechanism for melting can be understood by considering the motions of ions in the solid and liquid states. Prior to melting, the ions that constitute the metal remain relatively fixed in the vicinity of their equilibrium positions. As the metal is heated above the melting temperature, the ions acquire enough energy leave their equilibrium positions and wander relatively large distances, resulting in a liquid state. Melting of solid metal is a typical example of a first order phase transition. First order phase transitions are those in which the substance releases or absorbs heat energy during the phase change. Since the energy cannot be absorbed or released instantaneously by the substance at the phase transition temperature, first order phase transitions are characterized by a mixed phase regime in which different phases of the medium coexist.

To date, metallic phase transitions are widely investigated using calorimetry techniques, such as AC- calorimetry [7]. A disadvantage of this method is that an invasive physical contact is required to accurately measure heat flow through the metallic sample. To overcome this constraint, several groups [9, 12, 13] have employed the photo-acoustic effect to non-invasively probe metallic phase transformations. In such experiments, phase transition modulates the acoustic signal generated at the surface of a sample when a surrounding ambient gas has been heated by a periodically modulated light beam. However, such mechanism requires a gas that is highly absorbing to the illuminating light, and interpretation of the acoustic signal is restricted by the complex nature of heat transfer between the solid metallic sample and surrounding gas [13]. Gallium is a unique metallic element existing at room temperature as solid α-Ga consisting of a mixture of stable molecular and metallic phases. Solid α-Ga is a complex phase described as a metallic molecular crystal with strong Ga_2 bonds and weaker intermolecular forces, whereas liquid gallium is more free-electron like [4]. At a free-space wavelength of 1.55 μm, the permittivity of liquid gallium has been estimated to be approximately 7 times larger than the permittivity of α-Ga [10]. Gallium possesses one of the lowest melting points of all metals T_m = 29.8 C°, which provides an ideal platform to study metallic solid-liquid phase

transformation behavior via THz time-domain spectroscopy. Gallium particles are prepared by cooling bulk 99.99% gallium pellets to 77K and mechanically grinding the gallium pellets to achieve a powder having an average particle size of 109 ± 10 μm and a packing fraction of ~ 0.4 ± 0.1. In order to probe the phase transition of the gallium, THz time-domain spectroscopy in transmission mode is employed to monitor the effective optical properties of an ensemble of gallium particles as the temperature of the particles is raised past the melting point.

In the experimental setup, THz radiation is focused onto a polystyrene sample cell housing a L = 2.3mm thick collection of the random gallium particles. To examine the temperature-dependent THz transmissivity of the particles, the gallium particles are homogeneously heated, at a rate of 0.08 C°/min, from room temperature up to a temperature, T, of 38.2 C° (> T_m). Because the time over which the temperature increases is much longer than the heat diffusion time across the thin sample (< 1 s), it is ensured that the sample temperature is at equilibrium during the transmission measurements. The particles ensemble temperature is monitored (within ±0.1 C°) via a thermocouple inserted into the particle collection adjacent to the THz beam probing spot. During the measurements, both the beam spot size and location are kept fixed, thus ensuring that the THz radiation interacts with the same random realization of the particle ensemble throughout the temperature variation.

Melting is a thermal effect, and the temporal duration over which melting occurs is determined by the time over which heat can diffuse and equilibrate throughout the sample. The experiments are carefully designed and performed at an extremely slow heating rate (0.08 C°/min) in order to ensure that equilibrium conditions are established through the measurements. To quantify this condition, the heat diffusion times are estimated for both gallium metal (a lower bound) and air (an upper bound) through a distance of 2.3 mm corresponding to the sample thickness. Gallium has a thermal conductivity H_t = 40 WK^{-1}m^{-1}, a density u = 5910 kgm^{-3}, and a heat capacity C = 25.86 Jmol^{-1} K^{-1}. For air, H_t = 0.02WK^{-1}m^{-1}, u = 1.251 kgm^{-3} and C = 29.12 Jmol^{-1} K^{-1}. From these quantities, the thermal diffusivity is obtained from

$$D_t = H_t\, u^{-1}\, C^{-1}. \tag{5}$$

For a sample composed of gallium D_t = 1.9 × 10^{-5} m²/s and for a sample composed of air D_t = 9 × 10^{-6} m²/s. The characteristic diffusion time over a distance L is estimated by t_{diff} = L^2/D_t, yielding t_{diff} = 0.6 s for a sample composed entirely of gallium and t_{diff} = 0.28 s for a sample composed entirely of air. The sample used in the experiments is a mixture of air and gallium, and the characteristic heat diffusion time for the sample will lie between those bounds. To obtain an upper bound of time lagged thermal effects, we assume that it requires 0.6 s for heat to diffuse from one end of the sample to another. Over this time interval, a time-lagged temperature increase of 0.08 C°/min ×0.6 s = 0.0008 C°($\ll$ error in the temperature measurement) may develop across the sample. Since the time over which the temperature of the sample increases is much slower than the heat diffusion time across the sample thickness, it can be confidently concluded that the samples have reached thermal equilibrium as the THz time-domain spectroscopic measurements are taken. Fig. 13A illustrates the time-domain THz electric field waveforms, $E(t)$, transmitted through gallium particle collections measured at various temperatures. Notably, for temperatures below the melting point (T < T_m), the bipolar pulses transmitted through the particle collection all have an initial peak at a time t = 3.1 ps. The fact that the arrival delay, the amplitude, and the pulse shape of the transmitted pulses do not change throughout the temperature range 22.4 C° < T < 29.7 C° suggests an absence of

phase transformation or any changes to the gallium metallic properties. However, once the temperature reaches the melting temperature of 29.9 C°, a temporal advancement (or early arrival) of the pulse peak by 0.3 ps provides evidence of the onset of a significant transformation in the electronic properties of the gallium particles. Although the pulse corresponding to $T = T_m = 29.9$ C° is temporally advanced, interestingly, the pulse shape remains unaltered at T_m. Further heating of the gallium particles from 29.9 C° to 38.2 C° induces striking pulse shape transformation where the pulse is attenuated and broadened in time.
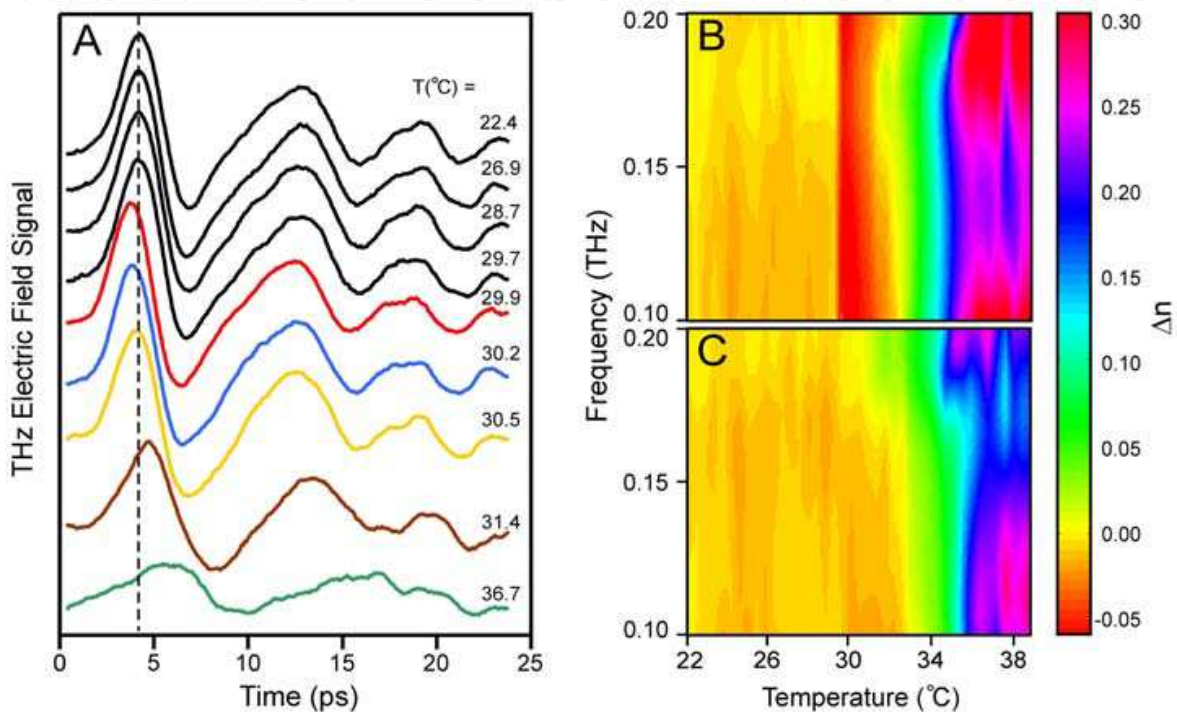

Fig. 13. (A) Experimental time-domain waveforms of THz pulses transmitted through 2.3-mmthick random gallium particle ensembles measured at various temperatures. The dashed line indicates the arrival time of the peak of the THz electric field pulse. Shown in (B) are the effective real refractive index change and (C) effective imaginary refractive index change versus temperature and frequency. The refractive indices are measured relative to the reference pulse transmitted through the sample at 21.2 C°.

Accompanying the temporal pulse shape trend with increasing temperature is a marked progressive delay and attenuation of $E(t)$. The pulse temporal shape, delay and amplitude trends for $T > T_m$ suggest conglomeration between adjacent, near-touching gallium particles. Because the THz transmission through the particle collections is mediated by nearest neighbor coupling between particles, conglomeration of the nearest-neighbor particles quenches radiation propagation mechanism. As the particles coalesce, the particles become larger and begin to exhibit metallic bulk-like electromagnetic properties, resulting in reduced transmission amplitude. Similarly, particle conglomeration results in a higher metal filling fraction, which increases the effective index of the particle ensemble and manifests as a temporal delay of the transmitted pulse.

To further explore the temperature-dependent evolution of the waveforms, the frequency-dependent relative effective refractive index inferred from the amplitude and phase of the transmitted THz electric fields relative to a reference THz electric field is analyzed. The effective real refractive index change

$$\Delta\mathrm{Re}[n] = \frac{\Phi(\omega) - \Phi_{ref}(\omega)}{kL} \tag{5}$$

and the effective imaginary refractive index change

$$\Delta\mathrm{Im}[n] = \frac{E(\omega)/E_{ref}(\omega)}{kL} \tag{6}$$

are obtained as a function of temperature, T. In these relations, $\Phi(\omega)$, $\Phi_{ref}(\omega)$, $E(\omega)$, and $E_{ref}(\omega)$ are the phase of the transmitted pulse, the phase of the reference pulse transmitted through the sample at T_{ref} = 21.2 C°, the amplitude of the transmitted pulse, and the amplitude of the reference pulse, respectively. Shown in Fig. 13B and 13C are $\Delta\mathrm{Re}[n]$ and $\Delta\mathrm{Im}[n]$ with respect to T over a frequency range between 0.1 THz and 0.2 THz (corresponding to the bandwidth of the transmitted pulse). As shown in the plot, there is negligible refractive index change between the temperature range 21.2 C° < T < T_m. At T_m = 29.9 C°, $\Delta\mathrm{Re}[n]$ decreases abruptly. As shown in Fig. 13B, this sharp discontinuity in $\Delta\mathrm{Re}[n]$ precisely at T_m is consistent over the entire transmission bandwidth. The abrupt, frequency-independent change in $\Delta\mathrm{Re}[n]$ suggests that the intrinsic electronic properties of gallium have been altered at T_m and is strongly indicative of metallic phase transformation. Interestingly, the onset of phase transition eludes detection in $\Delta\mathrm{Im}[n]$, as $\Delta\mathrm{Im}[n]$ remains approximately zero up to $T \simeq 30.5$ C°. With further increase in the sample temperature above 30.5 C°, both $\Delta\mathrm{Re}[n]$ and $\Delta\mathrm{Im}[n]$ show large increases over the transmission bandwidth as a function of T. These significant increases in the complex effective refractive indices of the ensemble show that the particle ensemble becomes less transparent to the THz pulse for $T > T_m$ due to coalescing of nearest-neighbor particles. The strikingly different effective refractive index features for the range $T < T_m$, $T \simeq T_m$, and $T > 30.5$ C° highlight three distinctive regimes where 1) the particles have not melted (constant $\Delta\mathrm{Re}[n]$ and $\Delta\mathrm{Im}[n]$), 2) the particles have melted but remain granular (discontinuity in $\Delta\mathrm{Re}[n]$, but constant $\Delta\mathrm{Im}[n]$), and 3) the particles have melted and are coalesced (large increases in both $\Delta\mathrm{Re}[n]$ and $\Delta\mathrm{Im}[n]$).

The temperature-dependent $\Delta\mathrm{Re}[n]$ and $\Delta\mathrm{Im}[n]$ trends at two frequencies, ω_1 = 0.1 THz and ω_2 = 0.2 THz are charted in Figs. 14A and 14B. As shown in Figure 14A, for 21.2 C° < T < 29.9 C°, $\Delta\mathrm{Re}[n]$ is nearly zero. Upon reaching T_m, the real part of the relative effective index exhibits a notably large, discontinuous jump of −0.06, indicative of an abrupt change in the intrinsic properties of gallium associated with metallic solid-liquid phase transformation. Above the melting temperature, $\Delta\mathrm{Re}[n]$ is strongly affected by conglomeration of the particles, which changes the underlying extrinsic microstructure of the ensemble. This extrinsic effect influences the effective index of the ensemble in a different way than the intrinsic metallic phase transition at T_m. For $T > T_m$, $\Delta\mathrm{Re}[n]$ increases from −0.06 to $\simeq 0.3$ between 29.9 C° and 33.0 C° and beyond $T > 33.0$ C°, is constant at $\simeq 0.3$. Particle conglomeration occurring at $T > T_m$ increases the effective real refractive index of the ensemble, causing the arrival delay of the transmitted pulses. $\Delta\mathrm{Im}[n]$ exhibits similar overall trends as $\Delta\mathrm{Re}[n]$. Below the melting temperature, $\Delta\mathrm{Im}[n]$ shows negligible temperature dependence and is approximately zero. As shown in Fig. 14B, $\Delta\mathrm{Im}[n(\omega_2)]$ increases linearly for $T > T_m$ and saturates at 0.2 for $T > 33.0$ C°. Such an increase in the imaginary effective refractive index reveals increased absorption or scattering losses within the ensemble due to

particle melting and subsequent coalescing. In contrast to $\Delta\text{Im}[n(\omega_2)]$, $\Delta\text{Im}[n(\omega_1)]$ does not significantly increase from zero until the temperature exceeds 30.5 C° > T_m. The slightly different trends observed for $\Delta\text{Im}[n(\omega_1)]$ and $\Delta\text{Im}[n(\omega_2)]$ suggest that the higher frequency components of the pulse are more sensitive to particle conglomeration than the lower frequency components. Overall, the real and imaginary parts of the complex effective index of the sample exhibit high sensitivity to the solid-liquid phase transition of the gallium particles and subsequent melting and coalescing dynamics beyond T_m.
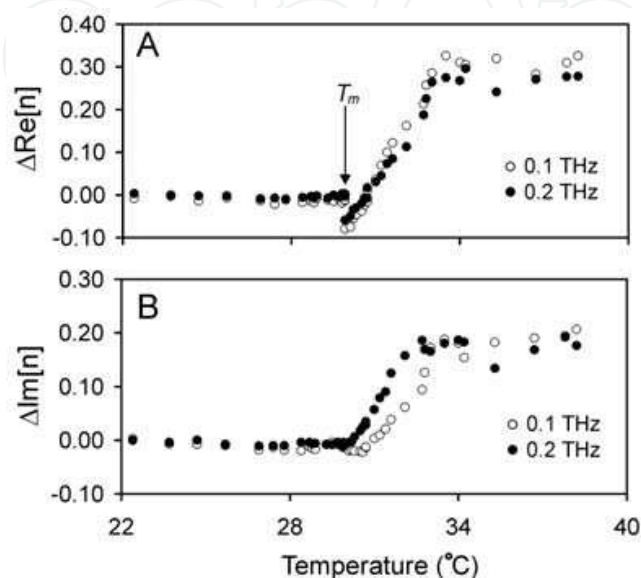

Fig. 14. Experimental effective (A) real refractive index change and (B) imaginary refractive index change at a frequency of 0.1 THz (empty circles) and 0.2 THz (filled circles) at various temperatures. The discontinuity in the effective real refractive index occurs at the gallium melting temperature, 29.8 C°.

The refractive index behavior for $T > T_m$ shows interesting particle conglomeration behavior of the gallium particles, where the particles begin to form interconnected networks. The experimental results show that coalescing does not occur concurrently with particle melting. To quantify the temperature where the particles begin to coalesce, the correlation function, $C(\tau) = \langle E(t+\tau)E_{ref}(t)\rangle$ is calculated, where $E(t+\tau)$ is the sample pulse (at a given temperature T) shifted by a time τ and $E_{ref}(t)$ is the reference pulse transmitted at reference temperature T_{ref}. It is noted that referencing the correlation function to the transmitted signal at T_{ref} cancels out the inherent spectral response of the setup since the spectral response of the system is fixed throughout the temperature variation. Because the only experimental variable is the sample temperature, changes in $C(\tau)$ as a function of T arise directly from temperature-dependent changes in the transmissivity of the gallium sample. As highlighted in the plot of the maximum correlation amplitude versus T [Fig. 15B], the transmitted pulse remains highly correlated even for T = 30.5 C° > T$_m$. Thus, at temperatures exceeding the melting transition, the extrinsic microstructure of the particle ensemble has not changed. However, at a coalescing temperature, T_c = 30.5 C°, there is a significant decrease in $C(\tau)$, marking the onset of particle conglomeration and transmission quenching. Because the particles must overcome their surface energy prior to liquefying, T_c is slightly higher than the bulk melting temperature. As shown in Fig. 15B, $C(\tau)$ decreases to 0.35 at 33.0 C°, and for $T >$

33.0 C°, the maximum correlation amplitude saturates and remains fixed. The experimental results reveal a narrow temperature range, $T_m < T < T_c$, where the individual particles have melted, yet the nearest-neighbor particles do not conglomerate.
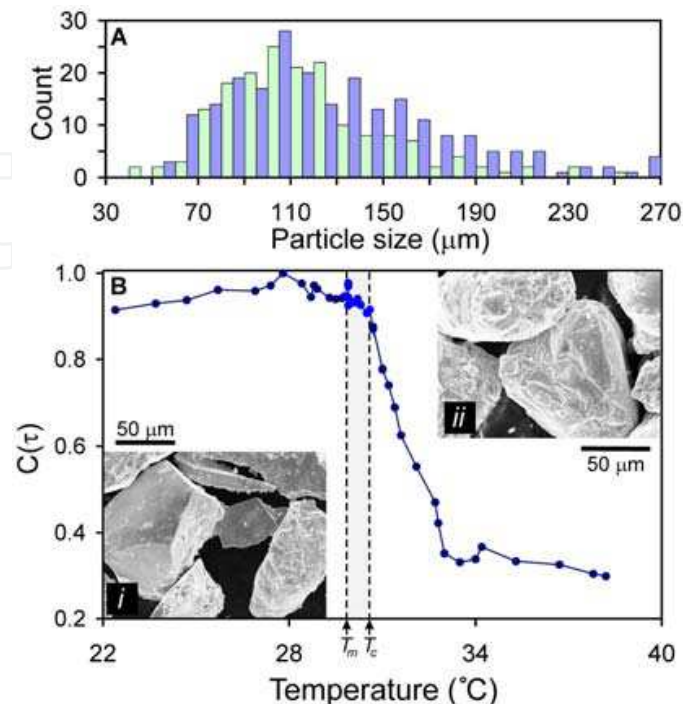

Fig. 15. (A) Size distribution of the gallium particles before melting (light bars) and after melting (dark bars). (B) shows the maximum correlation amplitude of transmitted pulses at various temperatures relative to the reference pulse at 21.2 C°. Insets are scanning electron microscope images of (i) the gallium particles prior to the heating cycle and (ii) the solidified particles after the heating cycle.

The gallium particle collection undergoes significant structural transformation over the heating cycle. After heating the particles above T_m and cooling back to room temperature, the nearest-neighbor particles have coalesced at small regions conjoining the particles, but overall, the ensemble retains a granular appearance and structure with no significant decrease in the total volume. The individual particles shapes are slightly distorted by the heating. As shown in the scanning electron microscope images in the insets of Fig. 15B, the particles prior to heating are characterized by sharp edges and flat faces. After cycling the temperature, the particles are rounded and have a rougher surface. Although heating induces shape change in the particles and coalescing between nearest-neighbor particles, the overall size distribution of the ensemble after heating is not significantly affected. As shown in Fig. 15A, the size distribution of the particles is nearly identical before and after heating. This further confirms that over the heating cycle, the particles do not fully conglomerate to form particles with augmented sizes. Rather, nearest-neighbor particles join at small sections of the particles that are in direct contact with each other.

6. Conclusion

THz time-domain spectroscopy has been employed to study the THz transparency of densely packed ensembles of subwavelength size metallic particles. Experimental

investigations of the THz transmission with respect to the sample length and particle size, with supporting evidence from numerical simulations based on FDTD calculations, indicate that the transmission is mediated by coherent, near-field electromagnetic coupling between nearest-neighbor particles. Transmission-based THz spectroscopy is applied as a non-invasive probe to study the phase transition of a metallic particle sample.

7. References

[1] C. F. Bohren and D. R. Huffman. *Absorption and Scattering of Light by Small Particles*. John Wiley & Sons, 1983.

[2] K. J. Chau, G. D. Dice, and A. Y. Elezzabi. Coherent plasmonic enhanced terahertz transmission through random metallic media. *Phys. Rev. Lett.*, 94:173904, 2005.

[3] K. J. Chau and A. Y. Elezzabi. Terahertz transmission through ensembles of subwavelength-size metallic particles. *Phys. Rev. B*, 72:075110, 2005.

[4] X. G. Gong, G. L. Chiarotti, M. Parrinello, and E. Tosatti. α-gallium: A metallic molecular crystal. *Phys. Rev. B*, 43:14277–14280, 1991.

[5] D. Grischkowsky, S. Keiding, M. v. Exter, and C. Fattinger. Far-infrared time-domain spectroscopy with terahertz beams of dielectrics and semiconductors. *J. Opt. Soc. B*, 7:2006–2015, 1990.

[6] S. C. Howells and L. A. Schlie. Transient terahertz reflection spectroscopy of undoped InSb from 0.1 to 1.1 THz. *Appl. Phys. Lett.*, 69:550–552, 1996.

[7] M. Kano. Adiabatic calorimeter for the purpose of calorimetry in the solid, liquid and supercooled phases of metals. *J. Phys. E*, 22:907–912, 1989.

[8] M. Khazan, I. Wilke, and C. Stevens. Surface impedance of T1-2212 thin films at THz-frequencies. *IEEE Trans. Appl. Super-cond.*, 11:3537–3540, 2001.

[9] P. Korpiun and R. Tilgner. The photoacoustic effect at first-order phase transition. *J. Appl. Phys.*, 51:6115–6119, 1980.

[10] A. V. Krasavin, A. V. Zayats, and N. I. Zheludev. Active control of surface plasmon-polaritons. *J. Opt. A*, 7:S85–S89, 2005.

[11] U. Kreibig and M. Vollmer. *Optical Properties of Metal Clusters*. Springer-Verlag, 1995.

[12] F. A. McDonald and G. C. Wetsel Jr. Generalized theory of the photoacoustic effect. *J. Appl. Phys.*, 49:2313–2322, 1978.

[13] E. V. Meija-Uriarte, M. Nararrete, and M. Villagran-Muniz. Signal processing in photoacoustic detection of phase transitions by means of the autospectra correlation-based method: Evaluation with ceramic $BaTiO_3$. *Rev. Sci. Instrum.*, 75:2887–2891, 2004.

[14] D. Mittleman. *Sensing with Terahertz Radiation*. Springer, 2003.

[15] D. M. Mittleman, R. H. Jacobsen, R. Neelamani, R. G. Baraniuk, and M. C. Nuss. Gas sensing using terahertz timedomain spectroscopy. *Appl. Phys. B*, 67:379–390, 1998.

[16] S. Mujumdar, K. J. Chau, and A. Y. Elezzabi. Experimental and numerical investigation of terahertz transmission through strongly scattering sub-wavelength size spheres. *Appl. Phys. Lett.*, 85:6284–6286, 2004.

[17] S. Nashima, O. Morikawa, K. Takata, and M. Hangyo. Measurement of optical properties of highly doped silicon by terahertz time domain reflection spectroscopy. *Appl. Phys. Lett.*, 79:3923–3925, 2001.

[18] A. Pashkin, M. Kempa, H. Nemec, F. Kadlec, and P. Kuzel. Phase-sensitive time-domain terahertz reflection spectroscopy. *Rev. Sci. Intrum.*, 74:4711–4717, 2003.

[19] V. M. Shalaev. Electromagnetic properties of small-particle composites. *Phys. Rep.*, 272:61–137, 1996.

Recent Optical and Photonic Technologies

Edited by Ki Young Kim

Research and development in modern optical and photonic technologies have witnessed quite fast growing advancements in various fundamental and application areas due to availability of novel fabrication and measurement techniques, advanced numerical simulation tools and methods, as well as due to the increasing practical demands. The recent advancements have also been accompanied by the appearance of various interdisciplinary topics. The book attempts to put together state-of-the-art research and development in optical and photonic technologies. It consists of 21 chapters that focus on interesting four topics of photonic crystals (first 5 chapters), THz techniques and applications (next 7 chapters), nanoscale optical techniques and applications (next 5 chapters), and optical trapping and manipulation (last 4 chapters), in which a fundamental theory, numerical simulation techniques, measurement techniques and methods, and various application examples are considered. This book deals with recent and advanced research results and comprehensive reviews on optical and photonic technologies covering the aforementioned topics. I believe that the advanced techniques and research described here may also be applicable to other contemporary research areas in optical and photonic technologies. Thus, I hope the readers will be inspired to start or to improve further their own research and technologies and to expand potential applications. I would like to express my sincere gratitude to all the authors for their outstanding contributions to this book.

How to reference

In order to correctly reference this scholarly work, feel free to copy and paste the following:

Kenneth J. Chau (2010). Terahertz Time-Domain Spectroscopy of Metallic Particle Ensembles, Recent Optical and Photonic Technologies, Ki Young Kim (Ed.), ISBN: 978-953-7619-71-8, InTech, Available from: http://www.intechopen.com/books/recent-optical-and-photonic-technologies/terahertz-time-domain-spectroscopy-of-metallic-particle-ensembles

INTECH
open science | open minds

www.intechopen.com